Fast-slow analysis of the Integrated Oscillator Model for pancreatic β-cells

Joseph P. McKenna[a], Richard Bertram[b,*]

[a] Laboratory of Biological Modeling, NIDDK National Institutes of Health Bethesda, MD 20892, United States
[b] Department of Mathematics and Programs in Molecular Biophysics and Neuroscience, Florida State University Tallahassee, FL 32301, United States

ARTICLE INFO

ABSTRACT

Insulin-secreting pancreatic β-cells are electrically excitable cells that are unusual because their electrical activity is influenced directly by metabolism via ATP-sensitive K^+ channels. At the same time, changes in the intracellular Ca^{2+} concentration that result from the cell's electrical activity influence metabolism in several ways. Thus, there is bidirectional coupling between the electrical dynamics and the metabolic dynamics in β-cells. A mathematical model has been previously developed, called the Integrated.
Oscillator Model (IOM), to highlight the bidirectional coupling involved in the oscillation mechanism. In this study, we show how this coupling can produce oscillations in β-cell activity. These oscillations have period similar to that of insulin secretion pulses observed in rats, mice, dogs, and humans, which has been shown to facilitate the action of the liver in maintaining glucose homeostasis. In a companion paper we show that the IOM can produce oscillations using two distinct mechanisms, depending on the values of electrical and metabolic parameters. In the present article, we use fast-slow analysis to understand the mechanisms underlying each of these oscillations. In particular, we show why a key variable in the glycolytic pathway generates a pulsatile time course in one type of oscillation, while it generates a sawtooth time course in the other type. The significance of these patterns is that the time course is a reflection of whether an intrinsic glycolytic oscillator is active, or whether the oscillations are a direct consequence of Ca^{2+} feedback onto glycolysis.

© 2018 Elsevier Ltd. All rights reserved.

1. Introduction

Clusters of endocrine cells in the pancreas, called islets of Langerhans, manage elevations in the blood glucose level such as after meals by secreting insulin into the blood stream, which enables tissue throughout the body to absorb glucose. Insulin is released from islet β-cells in pulses governed by periodic Ca^{2+} entry to the cytoplasm, caused by bursting electrical activity in the plasma membrane (Nunemaker and Satin, 2014). Pulsatile insulin secretion enhances the efficacy of the liver in glucose homeostasis (Bratusch-Marrain et al., 1986; Komjati et al., 1986; Matveyenko et al., 2012), and insulin pulsatility is impaired in patients with type 2 diabetes (Lillioja et al., 1993; O'Rahilly et al., 1988; Polonsky et al., 1988).

Despite a long history of β-cell modeling Sherman (2010), the interactions of intracellular pathways that maintain pulsatile insulin release are not fully understood. This is partly due to the challenge of synthesizing a coherent mechanism that includes the key features of glucose metabolism to adenosine triphosphate (ATP), membrane electrical activity, and the feedback of intracellular Ca^{2+} onto both. Unlike most electrially excitable cells, metabolism affects the cell's electrial activity via ATP-sensitve K^+ channels, which are inactivated by the nucleotide. Understanding rhythmogenesis in β-cells is also hindered by a lack of probes that can simultaneously monitor variables with high temporal resolution, particularly variables in glycolysis, the first phase of metabolism. In a recent article Merrins et al. (2016), we presented highly time-resolved records from glucose-stimulated β-cells of glycolytic metabolite (FBP: fructose 1,6-bisphosphate) levels, using a Förster resonance energy transfer (FRET) sensor attached to the enzyme pyruvate kinase (called PKAR) (Merrins et al., 2013), simultaneously with membrane potential (V) or the intracellular Ca^{2+} concentration. That study demonstrated that there are oscillations in glycolysis, as predicted by a mathematical model Bertram et al. (2004, 2007), but the sawtooth shape of the FBP oscillations was not as expected. This disconnect between model and data was resolved by including a known, but previously unincorporated, Ca^{2+} feedback at a key step of glucose metabolism Denton (2009), dramatically altering the FBP time course from pulsatile to the

sawtooth pattern observed experimentally (McKenna et al., 2016; Merrins et al., 2016). However, this change also brought about a transformation of the elements underlying rhythm generation, prompting a renaming of the modified model to the Integrated Oscillator Model (IOM) (Bertram et al., 2018). Understanding the dynamics underlying these oscillations is the goal of this article.

In a companion article Marinelli et al. (2018) we show that the IOM is capable of generating slow bursting electrical oscillations through two mechanisms that are indistinguishable if one only monitors the cell's electrical activity or intracellular Ca^{2+} level. However, the time course of the glycolytic variable FBP is pulsatile in one case and sawtooth in the other. The former reflects an intrinsic oscillation in the glycolytic subsystem, driven by positive feedback of FBP onto the enzyme that makes it, phosphofructokinase (PFK). This was described in Smolen (1995), which developed the model used for the glycolytic subsystem of the IOM. In contrast, the basis for the oscillations exhibiting a sawtooth FBP pattern remains unclear. As we show in Marinelli et al. (2018), in this situation the intrinsic glycolytic oscillator is not active. But then what drives the oscillations? This is important to know, since PKAR measurements reported thus far reflecting FBP levels have shown a sawtooth pattern. To answer this question we apply a fast-slow analysis Bertram and Rubin (2017) to a reduced version of the IOM, and then to the full IOM. We demonstrate how the Ca^{2+} feedback onto glycolysis drives the FBP time course. This is in contrast to the case of intrinsic glycolytic oscillations, where the regenerative PFK enzyme activity drives the FBP time course. The fast-slow analysis done here complements the analysis in the companion paper Marinelli et al. (2018) on the transitions between the two bursting mechanisms. It is also a mathematical realization of the mechanism described verbally and pictorially in Bertram et al. (2018).

2. The Integrated Oscillator Model

The IOM constsits of two modules, one for ATP production and the other for cellular electrical activity and calcium handling. Both are described in detail in the companion paper Marinelli et al. (2018) and are similar to the model used in an earlier study Bertram et al. (2004), except that in the current model there is Ca^{2+} feedback onto glycolysis. The full equations and parameters are given in the Appendix, with a more complete description given in the companion paper. The Appendix also contains a time scale analysis of the model variables. Computer codes are available for free download from http://www.math.fsu.edu/~bertram/software/islet.

2.1. Electrical activity and calcium handling

The electrical activity module of the IOM has a Hodgkin and Huxley (1952) formulation and is coupled to equations for the nucleotides adenosine diphosphate (ADP) and ATP, and to the intracellular Ca^{2+} concentration. It includes voltage-sensitive Ca^{2+} (I_{Ca}) and K^+ (I_K), Ca^{2+}-sensitive K^+ ($I_{K(Ca)}$), and ATP-sensitive K^+ ($I_{K(ATP)}$) ionic currents. The cell's membrane potential (V) is described by:

$$\frac{dV}{dt} = -\frac{1}{C}\left[I_{Ca} + I_K + I_{K(Ca)} + I_{K(ATP)}\right] , \tag{1}$$

where C is the membrane capacitance. Inward I_{Ca} and outward I_K are sufficient to generate continuous spiking whereas outward $I_{K(Ca)}$ and $I_{K(ATP)}$ act to restore electrical quiescence Bertram et al. (2004).

The cytoplasmic Ca^{2+} concentration, c, is determined by Ca^{2+} flux across the plasma (J_{mem}) and the endoplasmic reticulum (J_{er}) membranes:

$$\frac{dc}{dt} = f_{Ca}(J_{mem} - J_{er}), \tag{2}$$

where f_{Ca} is the fraction of Ca^{2+} ions not bound to buffers. The equations for the Ca^{2+} concentration in the endoplasmic reticulum (c_{er}) is:

$$\frac{dc_{er}}{dt} = f_{Ca}\sigma_{er}J_{er}, \tag{3}$$

where σ_{er} is the ratio of cytosolic volume to ER volume. The Ca^{2+} pumps in the ER membrane utilize energy from ATP to maintain the concentraion of Ca^{2+} in the ER at a much higher value than that in the cytosol. We assume that the mitochondrial Ca^{2+} concentration, c_m, is at equilibrium with the free cytoplasmic Ca^{2+} concentration, c, with proportionality constant $k_{Ca} = c_m/c \approx 5$ guided by Wiederkehr et al. (2011), thus $c_m = 5\,c$.

The Ca^{2+} flux terms are:

$$J_{mem} = -\left[\frac{\alpha}{V_{cyt}}I_{Ca} + k_{PMCA}c\right] \tag{4}$$

$$J_{er} = k_{SERCA}c - p_{leak}(c_{er} - c) . \tag{5}$$

Parameter V_{cyt} is the volume of the cytosolic compartment and α converts current to ion flux. The k parameters reflect the strength of Ca^{2+} pumps, while p_{leak} reflects the leak of Ca^{2+} across the ER membrane. Expressions for the ionic currents, including differential equations for activation variables, and parameter values are given in the Appendix and in Marinelli et al. (2018). This module has four differential equations.

2.2. Metabolism

The metabolism of glucose to ATP is very complex, and our model only contains the few necessary elements to produce oscillations in glycolysis and their downstream effect on ATP production. We use equations for glycolysis that are adapted from Smolen (1995) and qualitatively similar to Westermark and Lansner (2003). The key reaction, which is responsible for oscillations, is catalyzed by the allosteric enzyme phosphofructokinase (PFK). This reaction is the basis of rhythmogenesis in the glycolytic substem, as we illustrate later. Influx to glycolysis is through glucokinase (GK), which phosphorylates glucose to glucose 6-phosphate (G6P). Efflux from glycolysis is through the mitochondrial pyruvate dehydrogenase (PDH) complex, which decarboxylates the final glycolytic product pyruvate to supply acetyl CoA to the citric acid cycle, the next set of reactions in glucose metabolism. The glycolysis subsystem consists of two differential equations for the rates of concentration change of the PFK reaction substrate, fructose 6-phosphate (F6P), and product, fructose 1,6-bisphosphate (FBP):

$$\frac{dF6P}{dt} = 0.3(J_{GK} - J_{PFK}) \tag{6}$$

$$\frac{dFBP}{dt} = J_{PFK} - \tfrac{1}{2}J_{PDH}, \tag{7}$$

where the 0.3 factor is the assumed ratio of F6P to G6P in the cell (see Bertram et al. (2004)).

The glucokinase flux $J_{GK} = 0.001\ \mu M/ms$ is held constant to simulate perfusion of islets in constant stimulatory glucose. The PFK flux, J_{PFK}, is increased by its product FBP, creating positive feedback onto the enzyme catalysis. FBP is further metabolized by a chain of enzymatic reactions, assumed to be at quasi-equilibrium and represented through the flux term J_{PDH} (see McKenna et al. (2016) for details). Pyruvate dehydrogenase and several other dehydrogenases involved in the citric acid cycle are regulated by changes in the mitochodrial Ca^{2+} concentration, c_m Denton (2009). The PDH flux is described by:

$$J_{PDH} = V_{PDH}\ \sqrt{FBP}, \tag{8}$$

where $V_{PDH} = v_{PDH} s$ and s is a Ca^{2+}-dependent factor. We use V_{PDH} as a bifurcation parameter of the glycolytic subsystem in Figs. 3 and 4.

For most of the study we assume that the PDH flux rate responds instantaneously to c_m:

$$s = s_\infty(c_m) = \frac{c_m}{c_m + k_{PDH}^{Ca}} = \frac{c}{c + k_{PDH}^{Ca}/5} \quad (9)$$

with various values of the Ca^{2+} dissociation constant k_{PDH}^{Ca}. We later study the effects of non-instantaneous Ca^{2+} feedback, so the Ca^{2+} regulation of PDH is then modeled with a differential equation that describes first-order kinetics, with approach to equilibrium s_∞ with time constant τ_s:

$$\frac{ds}{dt} = \frac{s_\infty - s}{\tau_s}. \quad (10)$$

We use a phenomenological model for ADP and ATP, developed by Keizer and Magnus (1989) and used in Bertram et al. (2004). ATP production is driven by PDH flux and comes at the expense of ADP. The ADP concentration is given by:

$$\frac{dADP}{dt} = \frac{\left\{ ATP - \exp\left[\left(1 + 2.2\frac{J_{PDH}}{0.05 + J_{PDH}}\right)\left(1 - \frac{c}{0.35}\right)\right] ADP \right\}}{\tau_a}. \quad (11)$$

The dependence on the cytosolic Ca^{2+} concentration reflects the effect of Ca^{2+} flux across the mitochondrial inner membrane on the mitochondrial membrane potential Keizer and Magnus (1989). It is assumed that the sum of the cytosolic nucleotides is conserved, and that $AMP = ADP^2/ATP$ Smolen (1995), so

$$ATP = \frac{1}{2}\left[A_{tot} + \sqrt{-4ADP^2 + (A_{tot} - ADP)^2} - ADP\right]. \quad (12)$$

where A_{tot} is the total nucleotide concentration. We plot ATP rather than ADP since this nucleotide is more readily measured experimentally. There are three or four differential equations in the metabolic module, and all functional expressions and parameter values can be found in the Appendix and in the companion paper Marinelli et al. (2018).

3. Results

3.1. Ca^{2+} regulation of pyruvate dehydrogenase reshapes glycolytic oscillations

The IOM is based on the earlier Dual Oscillator Model, named to highlight the co-existence of oscillation mechanisms driven purely by the electrical/calcium module and those driven almost entirely by the metabolic module Bertram et al. (2007). The latter reflect the regenerative nature of fructose 1,6-bisphosphate (FBP) production by the allosteric enzyme phosphofructokinase (PFK), endowing the glycolytic subsystem Eqs. 6 and (7) with the capacity to oscillate. These oscillations, when they occur, drive oscillations in adenosine diphosphate (ADP) and adenosine triphosphate (ATP), which drive bursting oscillations in the cell's electrical activity through ATP-inactivated K(ATP) ion channels. The result, shown in Fig. 1A, is that the PFK substrate, fructose 6-phosphate (F6P), oscillates with a sawtooth pattern; the PFK product FBP oscillates with a pulsatile pattern; there is a burst of electrical impulses during each FBP pulse (drvien by an ATP pulse, not shown); and the electrical bursts bring Ca^{2+} into the cell resulting in c pulses. This scenario requires no Ca^{2+} feedback onto glycolysis, and in fact in Fig. 1A the Ca^{2+} feedback onto the pyruvate dehydrogenase (PDH) reaction is eliminated by setting the dissociation constant in Eq. (9) to zero, $k_{PDH}^{Ca} = 0$.

The mechanism for the glycolytic oscillations is illustrated in the (FBP,F6P) phase plane in Fig. 2A, which uses the glycolytic
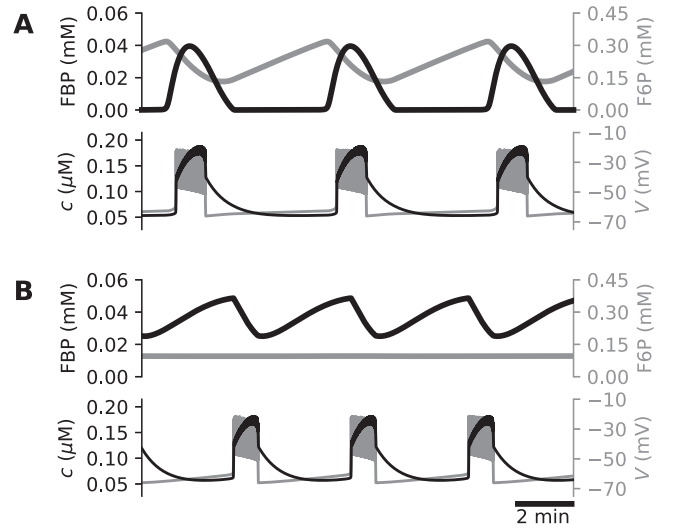

Fig. 1. Slow electrical bursting and Ca^{2+} oscillations can be produced through two very different mechanisms in the IOM. (A) Oscillations produced through the first mechanism are a result of oscillations in the glycolytic subsystem and exhibit pulses of FBP with a sawtooth F6P pattern. In this panel $k_{PDH}^{Ca} = 0$ so that the Ca^{2+} binding site on the PDH enzyme is saturated by Ca^{2+} (Eq. 9). (B) Oscillations produced by the second mechanism result in a sawtooth FBP pattern and no discernable F6P oscillations. In this panel mitochondrial Ca^{2+} feedback onto glycolysis is introduced by setting $k_{PDH}^{Ca} = 1$ µM so that the Ca^{2+} binding site on PDH is not saturated.
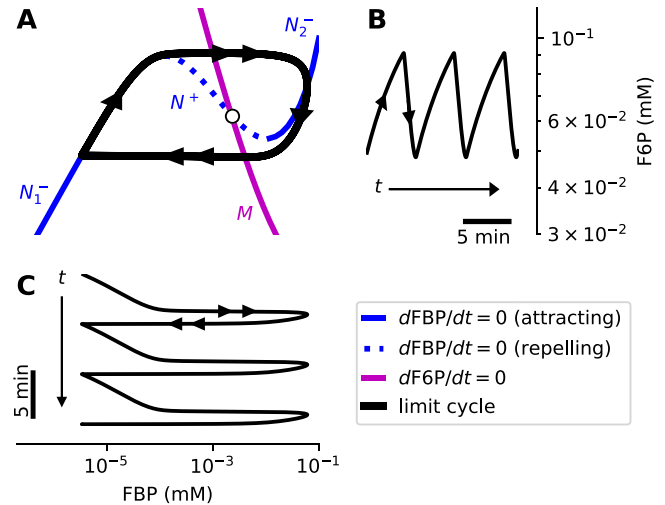
Fig. 2. One mechanism for slow oscillations in the IOM can be understood through an analysis of the glycolytic subsystem Eqs. 6 and (7), setting $s = 1$ and ATP = 2000 µM. (A) In the (FBP,F6P) phase plane, the limit cycle orbit moves along the outer branches (N^-) of the FBP nullcline with fast transitions (double arrow) between them. The F6P nullcline (M) intersects the FBP nullcline on its middle branch (N^+) at an unstable equilibrium. (B) F6P is the slow variable of the glycolytic subsystem, tracing out a sawtooth pattern. (C) FBP is the fast variable, with a square-wave or pulsatile timecourse.

subsystem Eqs. 6 and (7) in isolation. The FBP nullcline, satisfying $\frac{dFBP}{dt} = 0$, has a cubic shape, with left and right branches denoted as N^- and middle branch denoted as N^+. The F6P nullcline, $\frac{dF6P}{dt} = 0$ and labeled M, is nearly linear in the region of interest and intersects the FBP nullcline on N^+, resulting in an unstable equilibrium. A stable limit cycle is produced, whose orbit moves along the two branches of N^- except for nearly-horizontal fast transitions, tracing out a relaxation oscillation Bertram and Rubin (2017). In this two-timescale system, F6P is the slow variable and FBP is the fast variable (as shown in a time scale analysis in Appendix). As a result, the F6P timecourse has a sawtooth shape (Fig. 2B) while the FBP timecourse has more of a square-wave or
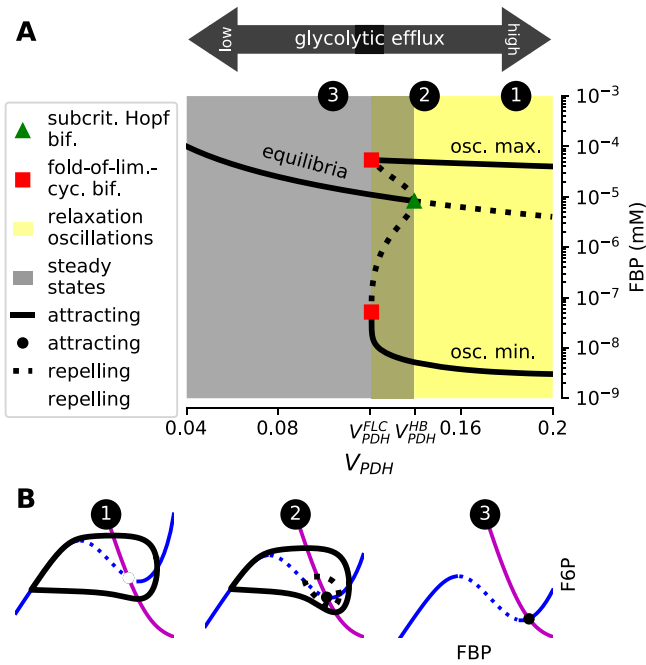
Fig. 3. Analysis of the isolated glycolytic subsystem, (Eqs. 6 and 7). (A) Bifurcation diagram with bifurcation parameter V_{PDH} and constant ATP = 2000 μM. The limit cycle attractor depicted in Fig. 2A disappears by a fold-of-limit-cycles bifurcation at $V_{PDH} = V_{PDH}^{FLC}$ where it coalesces with a limit cycle repeller that emerges at a subcritical Hopf bifurcation when $V_{PDH} = V_{PDH}^{HB}$. (B) The (FBP, F6P) phase plane has a globally attracting limit cycle for $V_{PDH} > V_{PDH}^{HB}$, a globally attracting equilibrium for $V_{PDH} < V_{PDH}^{FLC}$, and is bistable for $V_{PDH}^{FLC} < V_{PDH} < V_{PDH}^{HB}$.

pulsatile shape (Fig. 2C). This mechanism for rhythmogenesis carries through in the full IOM model, with the F6P and FBP time-courses showing the same patterns as in the isolated glycolytic subsystem.

Slow bursting oscillations can be produced in a very differenet way, as illustrated in Fig. 1B. In this case, the electrical bursts and Ca²⁺ pulses look just as they did in the first case. However, now the F6P oscillations are tiny, and not visible in the figure, while the FBP time course has a sawtooth pattern. The mechanism driving these oscillations is fundamentally different from that above, and in particular is not based on regenerative FBP production through the PFK enzyme. The switch from one mechanism to the next was achieved through a change in a single parameter: the dissociation constant k_{PDH}^{Ca} was changed from 0 to 1 μM. This has the effect of introducing Ca²⁺ feedback onto glycolysis via the activating action of mitochondrial Ca²⁺ onto the PDH reaction (Eq. 9). Understanding the mechanisms for this transition and the sawtooth FBP oscillations are the goals of this paper.

3.2. Analysis of the glycolytic subsystem reveals the influence of feedback on rhythmogenesis

The glycolytic subsystem is a conditional oscillator. The activation state of the oscillator is determined by the values of two inputs to the subsystem, the PDH flux rate V_{PDH} and the ATP concentration. Fig. 1 demonstrated that introducing Ca²⁺ feedback onto glycolysis can terminate intrinsic glycolytic oscillations in the full model through its effect on V_{PDH}. In this section, we explore the effects of input to the glycolytic subsystem in isolation Eqs. 6 and (7), by systematically investigating the influence of both V_{PDH} and ATP on the state of the conditional oscillator. We then examine the values of V_{PDH} and ATP produced in the full model during slow bursting, using what we learned from the isolated glycolytic sub-
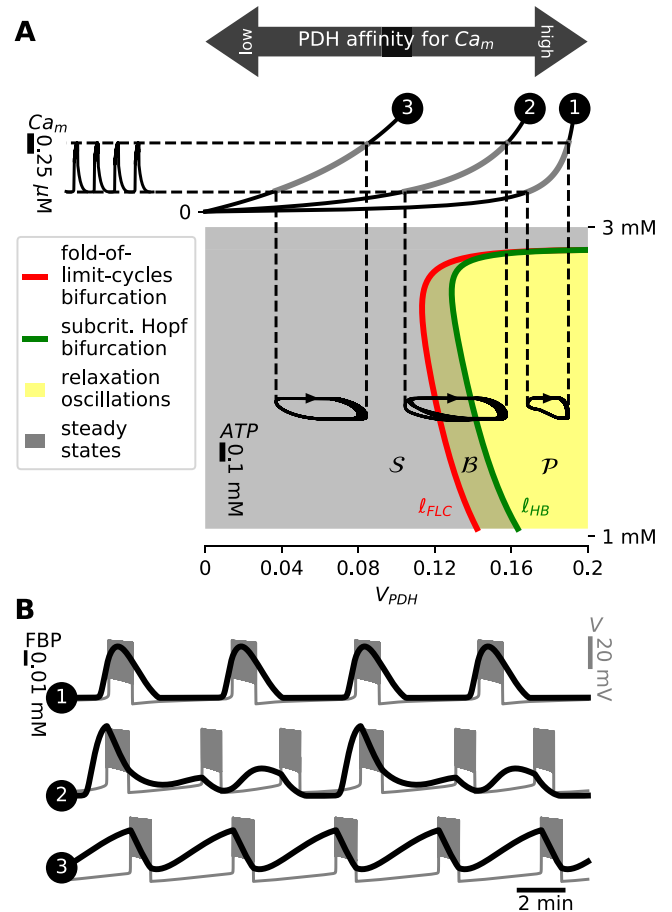
Fig. 4. Ca²⁺ regulation of PDH reshapes glycolytic oscillations. (A) A two-parameter (V_{PDH} and ATP) bifurcation diagram of the glycolytic subsystem, with slow bursting trajectories of the full IOM superimposed. c_m oscillations generated by the IOM (top left) feed back onto glycolysis through the Michaelis-Menten factor $s = s_\infty(c_m)$ (Eq. 9) (top right) of the PDH flux function (Eq. 8). The glycolytic oscillator is activated in region $\mathcal{P}$, where it produces periodic oscillations. It is inactivated in region $\mathcal{S}$, where it has a stable steady state. In region $\mathcal{B}$ it is bistable, with both stationary and periodic solutions. In case 1, the IOM projection lies entirely in region $\mathcal{P}$, while in case 3 it lies entirely in region $\mathcal{S}$, and in case 2 it lies in region $\mathcal{B}$. (B) As k_{PDH}^{Ca} is increased, i.e., PDH affinity for Ca²⁺ is decreased, the IOM trajectories move from $\mathcal{P}$ (A1) through $\mathcal{B}$ (A2) to $\mathcal{S}$ (A3), resulting in pulsatile (B1), mixed-mode (B2), and sawtooth (B3) FBP oscillations. (For interpretation of the references to color in this figure, the reader is referred to the web version of this article.).

system to interpret the metabolic oscillations produced by the full model.

We begin by fixing ATP at 2000 μM and doing a bifurcation analysis of Eqs. 6 and 7 with bifurcation parameter V_{PDH}. As V_{PDH} is lowered from its maximum value v_{PDH}, the equilibrium gains stability at a subcritical Hopf bifurcation ($V_{PDH} = V_{PDH}^{HB}$ in Fig. 3A) and gives rise to an unstable limit cycle that coalesces with and annihilates a stable limit cycle at a fold-of-limit-cycles bifurcation ($V_{PDH} = V_{PDH}^{FLC}$ in Fig. 3A). For $V_{PDH} \in [V_{PDH}^{FLC}, V_{PDH}^{HB}]$ the glycolytic subsystem is bistable, with coexisting stable stationary and periodic solutions. For $V_{PDH} < V_{PDH}^{FLC}$ the periodic solutions are no longer present, so the stable equilibrium is globally attracting. The effects of V_{PDH} on structures in the glycolytic phase plane are illustrated in Fig. 3B, with labels indicating the different positions in the bifurcation diagram. Label 1 reflects the case of moderately high glycolytic flux, with V_{PDH} near v_{PDH}, while label 3 reflects the case of low glycolytic flux due to the reduced PDH activity with a lower V_{PDH} value (Eq. 8).

How do the bifurcations depicted in Fig. 3A change as ATP is varied? The Hopf and fold-of-limit-cycles bifurcations continue in

the (V_{PDH}, ATP)-plane as curves ℓ_{HB} and ℓ_{FLC} (Fig. 4A, green and red, respectively). In the region to the right of ℓ_{HB} (denoted $\mathcal{P}$) there are globally attracting limit cycles. In the region to the left of ℓ_{FLC}, denoted $\mathcal{S}$, there are globally attracting equilibria. Between the two bifurcation curves, region $\mathcal{B}$, the system has coexisting stable stationary and periodic solutions.

Having classified regions of the (V_{PDH}, ATP)-plane according to the glycolytic subsystem's attractors, we next examine which regions the IOM trajectories explore as the strength of Ca^{2+} feedback onto metabolism is varied. In the IOM, periodic bursting electrical activity brings Ca^{2+} into the cytoplasm that subsequently enters the mitochondrial matrix. That is, bursting drives mitochondrial Ca^{2+}, c_m, oscillations (Fig. 4A, top left) that regulate glycolytic efflux through the Michaelis-Menten function $s = s_\infty(c_m)$ with half-activation constant k_{PDH}^{Ca} (Eq. 9). As k_{PDH}^{Ca} is increased, the affinity of PDH for c_m decreases and s_∞ becomes less steep (Fig. 4A, top right), in particular $\frac{ds_\infty}{dt}(0) = 1/k_{PDH}^{Ca}$. Since s_∞ is monotonic, it maps $[\min_t c_m, \max_t c_m]$ to $[s_\infty(\min_t c_m), s_\infty(\max_t c_m)]$. Since $V_{PDH} = v_{PDH}s_\infty$, the range of values taken on by V_{PDH} during bursting is proportional to the range of values taken on by s_∞, and is indicated by dashed lines in Fig. 4A. Then, the projection of the trajectory of the full IOM into the (V_{PDH}, ATP)-plane explores only $\mathcal{P}$ if $v_{PDH}s_\infty(\min_t c_m(t))$ is to the right of ℓ_{HB}, as in case 1 (Fig. 4A1). That is, in this case the input to the conditional glycolytic oscillator is entirely in a region in which the oscillator is activated, so intrinsic glycolytic oscillations should be produced. Evidence that this in fact occurs is given in Fig. 4B1, which shows the pulsatile FBP oscillations characteristic of the isolated glycolytic oscillator (Fig. 2). The IOM explores only $\mathcal{S}$ if $v_{PDH}s_\infty(\max c_m(t))$ is to the left of ℓ_{FLC}, as in case 3 (Fig. 4A3). In this case, the input to the conditional glycolytic oscillator is such that it is not activated, so any oscillations in the glycolytic variables involve interactions with the other components of the IOM, particularly the cytosolic Ca^{2+} concentration. This is shown in (Fig. 4B3), where the FBP level exhibits a sawtooth, rather than pulsatile, pattern. Finally, in case 2 the IOM explores more than one of $\mathcal{P}$, $\mathcal{B}$, and $\mathcal{S}$ for intermediate k_{PDH}^{Ca} and mixed mode oscillations are produced (Fig. 4B2). We do not explore these oscillations further, but instead focus on those of the type produced in case 3.

3.3. The basis of sawtooth FBP oscillations through the lens of a reduced model

When the c_m feedback parameter k_{PDH}^{Ca} is small, the IOM produces pulsatile FBP oscillations, since in this case the intrinsic glycolytic oscillator is activated (Fig. 4). In this section and the next, we address the mechanism for the sawtooth FBP oscillations that can occur when the intrinsic glycolytic oscillator is not active. We begin the analysis using a reduced version of the IOM that provides useful insights that are applied to the analysis of the full IOM in the next section. The idea behind the model reduction is to keep the glycolytic subsystem and the dynamics of the s variable (which we rename σ in the reduced model), while removing the electrical and Ca^{2+} components of the IOM. To do this, the dependence of s_∞ on c_m must be replaced so that it depends on either F6P or FBP. In the full IOM with small k_{PDH}^{Ca}, $s = s_\infty(c_m)$ oscillations are nearly square pulses that are in phase with FBP (Fig. 5). Thus, the most natural approach is to make the s equilibrium function for the reduced model, which we denote by σ_∞, produce a similar square wave pattern. This is achieved by defining σ_∞ as a function of FBP such that when FBP is past a threshold σ_∞ is set to some σ_{max} and when FBP is below the threshold σ_∞ is set to some σ_{min}:

$$\sigma_\infty(FBP, \sigma) = \begin{cases} \sigma_{min} & \text{if } FBP < T(\sigma) \\ \sigma_{max} & \text{if } FBP \geq T(\sigma), \end{cases} \quad (13)$$
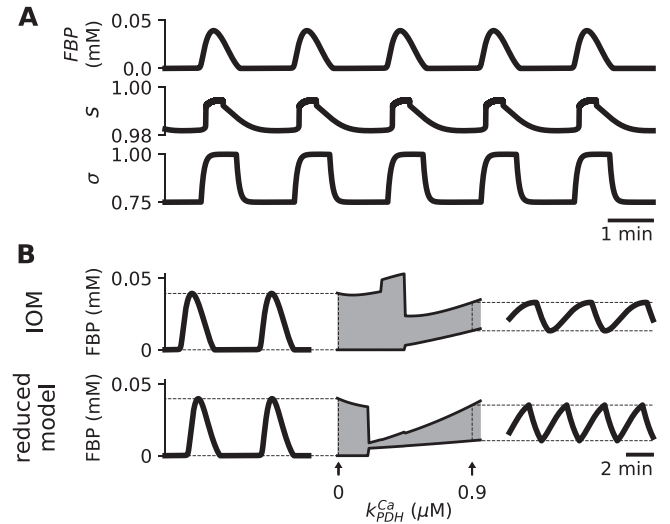
Fig. 5. Dynamics of the reduced model compared with those of the IOM. (A) For small k_{PDH}^{Ca} ($=0$ here) the IOM produces FBP pulses (top) in phase with square-wave-like s (middle) oscillations, and the reduced model (Eqs. 15–17) produces square-wave-like σ oscillations (bottom) that capture the behavior of the full model. (B) The range of FBP oscillations produced by the IOM and reduced model under variations in k_{PDH}^{Ca} (center). Both models produce FBP pulses (left, with $K_{PDH}^{Ca} = 0$) and sawtooth-like FBP oscillations (right, with $K_{PDH}^{Ca} = 0.9$) in small and large k_{PDH}^{Ca} regimes, respectively. The middle panel illustrates the range of FBP values attained during oscillations at each value of k_{PDH}^{Ca}. Note the large drop in amplitude in both models when the FBP oscillations switches from a pulsatile to a sawtooth pattern.

where the threshold T depends on σ and is the equilibrium value of FBP as a function of s (now called σ) in Eqs. 6 and 7. Thus,

$$T(\sigma) = \left(\frac{2J_{GK}}{\sigma \, v_{PDH}}\right)^2. \quad (14)$$

With this formulation, the reduced model is:

$$\frac{d\sigma}{dt} = \frac{\sigma_\infty(FBP, \sigma) - \sigma}{\tau_\sigma} \quad (15)$$

$$\frac{dF6P}{dt} = 0.3(J_{GK} - J_{PFK}) \quad (16)$$

$$\frac{dFBP}{dt} = J_{PFK} - \frac{1}{2}J_{PDH}(FBP, \sigma), \quad (17)$$

where the dependence of J_{PDH} on FBP and σ, rather than s, is highlighted. The oscillations produced by this reduced model have the same pulsatile FBP time course, with parallel pulses of σ that are qualitatively similar to those of s generated by the full IOM (Fig. 5A).

The reduced model depends on the parameters σ_{min}, σ_{max}, and τ_σ but not k_{PDH}^{Ca}. However, the values of these parameters can be set to reflect the effects of k_{PDH}^{Ca} on the full IOM, thereby facilitating comparison of the dynamics produced by the two models. We achieve this by setting σ_{min} and σ_{max} in the reduced model to the asymptotic values of $\min_t s(t)$ and $\max_t s(t)$ recorded in the IOM simulation with the corresponding k_{PDH}^{Ca}. We set τ_σ to the exponential decay time constant of s from $\max_t s(t)$ when all other IOM state variables are frozen at a time that s achieved $\max_t s(t)$. Using this approach, Fig. 5B depicts the range of FBP oscillations generated by the IOM and the reduced model as a function of k_{PDH}^{Ca}. The IOM and the reduced model both produce FBP pulses for small k_{PDH}^{Ca} (Fig. 5B, left) and sawtooth-like FBP oscillations for large k_{PDH}^{Ca} (Fig. 5B, right). The minimum and maximum of the FBP oscillations as functions of k_{PDH}^{Ca} are shown in the middle portion of Fig. 5B. This panel demonstrates that the amplitude changes with a
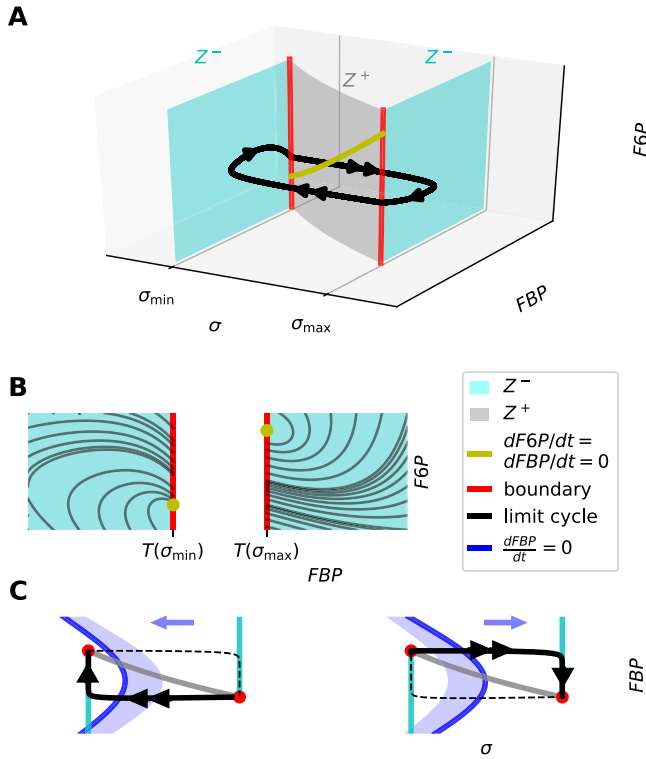
Fig. 6. The mechanism for sawtooth FBP oscillations in the large k_{PDH}^{Ca} regime (here $k_{PDH}^{Ca} = 1$ μM) of the reduced model (Eqs. 15–17). (A) A limit cycle (black) moves along the attracting half-planes of Z^- except for fast jumps between the two sheets. (B) The flow of the slow (F6P,FBP) subsystem along the $\sigma = \sigma_{min}$ half-plane (left, black curves) and along the $\sigma = \sigma_{max}$ half-plane (right, black curves) moves up to the boundary (red). Before it can reach the equilibrium (yellow), the trajectory reaches the boundary lines (red) and rapidly jumps to the other sheet. (C) A cross section of panel A for fixed F6P, with projections of segments of the limit cycle orbit. Also included is the FBP nullcline (dark blue) which is parameterized by σ, forming shadows (light blue). (For interpretation of the references to colour in this figure legend, the reader is referred to the web version of this article.)

rapid transition corresponding to the passage from an active intrinsic glycolytic oscillator to an inactive state (and a transition from the $\mathcal{P}$ region to the $\mathcal{S}$ region in Fig. 4). Overall, the FBP dynamics generated by the reduced model capture those of the IOM over the full range of k_{PDH}^{Ca}.

We characterize the mechanism for sawtooth-like FBP oscillations in the large k_{PDH}^{Ca} regime by applying fast-slow analysis to the reduced model, treating σ as the fast variable and F6P and FBP as slow variables (though F6P changes more slowly than FBP). The critical manifold, or fast-subsystem equilibria, is the σ-nullcline

$$Z^- = \{(\sigma, F6P, FBP) \in \mathbb{R}^3 : \sigma_\infty(FBP, \sigma) - \sigma = 0\} \quad (18)$$

of Eq. (15), which consists of two half-planes (Fig. 6, cyan) that contain the stable equilibria of Eq. (15) with F6P and FBP treated as parameters. The threshold sheet (Fig. 6, gray)

$$Z^+ = \{(\sigma, F6P, FBP) \in \mathbb{R}^3 : T(\sigma) = FBP\} \quad (19)$$

behaves as a repelling sheet in the fast subsystem since σ approaches σ_{min} when σ is on one side of the sheet and approaches σ_{max} when on the other side.

The orbit of the sawtooth FBP oscillation follows close to the two sheets of the critical manifold Z^- except for rapid transitions from one to the next (Fig. 6A). These transitions occur when the phase point reaches the boundary (red) where Z^- and Z^+ meet. The boundary lines of the attracting sheets are shown in red in Fig. 6.

The slow subsystem Eqs. 16 and (17) has equilibria parameterized by $\sigma \in [\sigma_{min}, \sigma_{max}]$ (yellow curve in Fig. 6A and yellow points
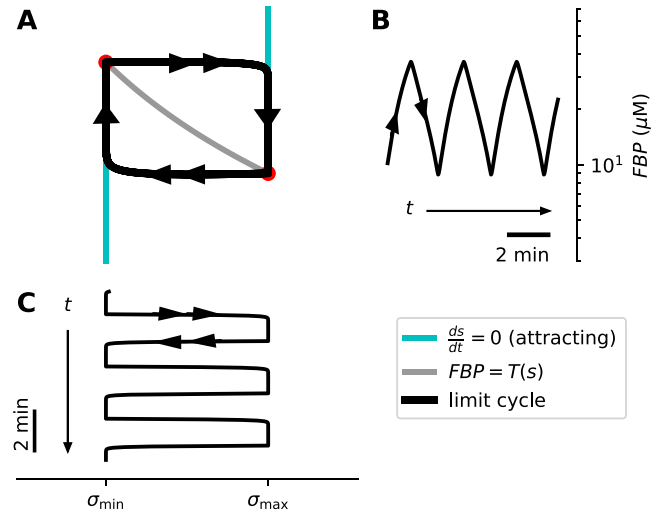
in Fig. 6B), such that at σ_{min} the equilibrium lies on the boundary line of the σ_{min} sheet and at σ_{max} it lies on the boundary line of the σ_{max} sheet. In each case, the equilibrium is a stable focus of the slow flow. The flow of the slow subsystem (black curves in Fig. 6B) on either sheet of Z^- moves towards the equilibrium point but intersects the boundary line before reaching it (Fig. 6B), at which time there is a rapid transition to the other sheet of Z^-. Thus, the system never reaches equilibrium and instead converges to a periodic attractor.

As in the small k_{PDH}^{Ca} regime, the dynamics of the reduced model in the large k_{PDH}^{Ca} regime are approximately planar. In contrast to the small k_{PDH}^{Ca} regime for which the important dynamics appear in the (FBP,F6P)-plane, the important dynamics in the large k_{PDH}^{Ca} regime appear in the (σ, FBP)-plane (Fig. 6C), where it becomes important that F6P changes more slowly than the other two variables. The limit cycle trajectory moves along the projection of Z^-, with vertical direction dictated by whether the phase point is to the left or the right of the FBP nullcline (dark blue curve). To the left of the FBP nullcline FBP increases, while it decreases to the right. The FBP nullcline that is shown is actually a projection, parameterized by σ: the nullcline moves leftward when $FBP(t) < T(\sigma(t))$ and rightward when $FBP(t) > T(\sigma(t))$, as indicated by the arrows. The past history of the nullcline is indicated as light blue shadows, while the dark blue curves indicate the positions of the nullclines when the phase point reaches a boundary point. When the phase point reaches a boundary point (red circles) it makes a rapid jump from one sheet of Z^- to the other. This is a relaxation oscillation, with σ acting as a fast variable and therefore exhibiting square-wave pulses, and FBP acting as a slow variable and thus exhibiting a sawtooth pattern (Fig. 7). These oscillations occur even if the F6P variable is frozen at an appropriate value, so they are truly an interaction between the fast σ variable and the slower FBP variable. Time-dependent changes in the slowest variable, F6P, play no role.

Fig. 7. (A) Relaxation oscillations of the reduced model (Eqs. 15–17) in the large k_{PDH}^{Ca} regime (here $k_{PDH}^{Ca} = 0.9$ μM). (B) The FBP timecourse has a sawtooth pattern since it is a slow variable. (C) The σ timecourse is pulsatile since it is a fast variable.

3.4. Sawtooth FBP oscillations in the IOM

We now move to the more complex IOM, seeking to understand how the oscillation mechanism in the reduced model follows through to the full model, and also determining the role played by ATP, which is not included in the reduced model. Unlike the reduced model, in the IOM the dynamics of s are a product of the electrical activity module of the IOM. We again use a fast-slow
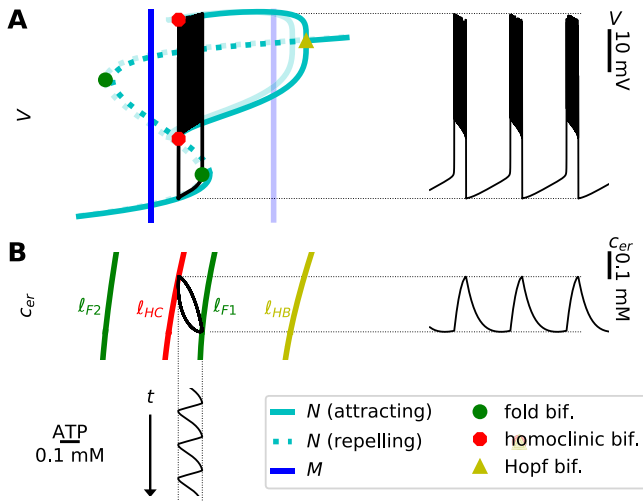
Fig. 8. Fast-slow analysis of bursting in the IOM. (A) The bursting trajectory (black) superimposed on the fast-subsystem bifurcation diagram, shown at the maximum value of c_{er} during the oscillation (dark cyan) and the minimum value (light cyan). Fold bifurcations (green), a homoclinic bifurcation (red), and a supercritical Hopf bifurcation (yellow) are all labeled. Also shown is the bursting V time course. (B) The codimension-1 bifurcations of panel A continued for the range of c_{er} values taken on during the oscillation form increasing curves in the (ATP,c_{er})-plane. Also shown are the c_{er} and ATP timecourses. (For interpretation of the references to colour in this figure legend, the reader is referred to the web version of this article.)

analysis, but now with more fast and more slow variables. We categorize V, n, and c as fast variables, c_{er} and FBP as variables that change on a medium time scale, and F6P and ATP as slow variables. We also note again that ATP is related to ADP by an algebraic equation (Eq. 37), and ADP evolves through a differential equation (Eq. 11). Both ADP and ATP evolve on slow time scales. The analysis is simplified by the fact that the fast subsystem depends on only two of the slow variables, ATP (or ADP) and c_{er}.

Fig. 8 shows a bifurcation diagram of the fast subsystem, with c_{er} clamped and ATP used as a bifurcation parameter. At large values of ATP there is a high-V branch of stable equilibria of the fast subsystem. As ATP is decreased this branch loses stability at a supercritical Hopf bifurcation (HB, solid yellow triangle), giving rise to a branch of stable periodic solutions. Each periodic solution is a continuous train of electrical impulses, and the minimum V of the impulses is shown as a lower branch while the maximum V of the impulses forms an upper branch. The periodic solutions terminate at a homoclinic bifurcation (HC, solid red circles) when the periodic branch reaches a branch of saddle points. The saddle points exist between two saddle-node or fold bifurcations (solid green circles). The rightmost fold bifurcation is denoted F1, while the other is denoted F2. At bifurcation F1 the middle branch of saddle points folds back and creates a branch of stable equilibria that forms the bottom branch of the s-shaped fast-subsystem bifurcation diagram. There are actually two bifurcation diagrams shown in Fig. 8A; the dark cyan diagram corresponds to c_{er} fixed at the value reached at the end of the burst active pahse, while the light cyan diagram corresponds to c_{er} fixed at the value reached at the end of the burst silent phase.

We next superimpose the projection of the bursting orbit (black curve) onto the fast-subsystem bifurcation diagram N, now thinking of the (ATP,V)-plane as a phase plane. The phase point travels along N except for jumps between attracting structures, because of the time scale separation between the fast variables and ATP. During a burst active phase the phase point moves leftward towards the projection of the ATP nullcline (M, dark blue line). This nullcline satisfies $\frac{dADP}{dt} = 0$ where $\frac{dADP}{dt}$ is given in Eq. (11), and then ATP is obtained from Eq. 37. Since this expression does not contain

V, the nullcline is a vertical line in the (ATP,V) plane. However, the nullcline does depend on s, which is a function of c_m, assumed to be at equilibrium with c. Hence, when the active phase trajectory reaches the HC bifurcation and spiking stops, there is no Ca^{2+} influx and c_m rapidly declines which causes s to decline and the ATP nullcline to rapidly shift rightward (light blue vertical line). Now, during the burst silent phase, the phase point moves slowly rightward towards the ATP nullcline until it reaches the fold bifurcation F1. At this point a new active phase is initiated, raising c_m and subsequently s, shifting the ATP nullcline leftward again. This series of slow motions of the phase point along the critical manifold and fast motions of the ATP nullcline when HC and F1 bifurcations are reached produce the electrical bursting oscillations of the IOM.

The other slow variable, c_{er}, influences the bursting by slowly shifting the fast system bifurcation diagram N rightward during a burst active phase and leftward during a silent phase. The left-right motion of N can be summarized by continuing its codimension-1 bifurcations in the (ATP,c_{er})-plane (Fig. 8B). These bifurcations continue as increasing curves, reflecting the fact that N moves rightward as c_{er} increases. When the burst is projected into this plane it forms a closed loop with clockwise orientation between a curve of fold bifurcations (ℓ_{F1}) and the curve of homoclinic bifurcations (ℓ_{HC}). The fast variable V exhibits a bursting oscillation (Fig. 8A) while both of the slow variables ATP and c_{er} exhibit sawtooth oscillations (Fig. 8B).

We have so far demonstrated why ATP exhibits a sawtooth pattern during bursting, but why does FBP also have such a pattern? To see this we view the bursting in the (s, FBP)-plane. To do this, we make the approximation $\frac{dF6P}{dt} = 0$ since F6P is nearly constant in the large k_{PDH}^{Ca} regime (Fig. 1B) and use the resulting relation $J_{GK} - J_{PFK}(F6P, FBP, ATP) = 0$ to write FBP in terms of ATP and F6P. We then replot N in the (s, FBP)-plane.

The sawtooth FBP and ATP time courses that occur during bursting are shown in Fig. 9A, with labels attached to different time points. Fig. 9B depicts N (cyan), M (blue), and portions of the bursting orbit (black) in the (s, FBP)-plane with ATP and c_{er} fixed at their values during the labeled time points. The left branch of stable equilibria in Fig. 9B corresponds to the bottom branch of stable fast-subsystem equilibria depicted in Fig. 8A. The min/max curves of s in the right portion of each diagram in Fig. 9B correspond to the min/max V curves for the fast-subsystem spiking solutions in Fig. 8A.

During the silent phase (Fig. 9, left), the trajectory (segment shown in black) of the bursting attractor (gray) moves towards (labels 1 and 2) and then along (label 3) the small s equilibria curve before passing a fold bifurcation and moving rapidly towards the periodic spiking branch (label 4). This starts the burst active phase (Fig. 9B, right), during which the trajectory moves slowly along the periodic branch (labels 5 and 6) before passing the homoclinic bifurcation (solid red circles) and moving rapidly back to the equilibria curve (label 1). The mechanism depicted in Fig. 9B is similar to the mechanism for sawtooth FBP oscillations of the reduced model (Fig. 6) in that the periodic orbit moves slowly along and jumps between solution curves of the fast subsystem at small and large s values and that the slow-subsystem nullcline moves leftward during the silent phase and rightward during the active phase (blue curve and shadow in Fig. 9B). The motion of the bursting orbit in Fig. 9B produces sawtooth FBP oscillations and square-wave-like s oscillations, just as with the reduced model.

3.5. Ca^{2+} regulation of pyruvate dehydrogenase must be rapid

Up to this point, we have only considered PDH that responds instantaneously to Ca^{2+} concentration changes by setting $s = s_\infty(c_m)$. In that case, we found that setting the dissociation constant k_{PDH}^{Ca} in the Michaelis-Menten function $s_\infty(c_m)$ to larger
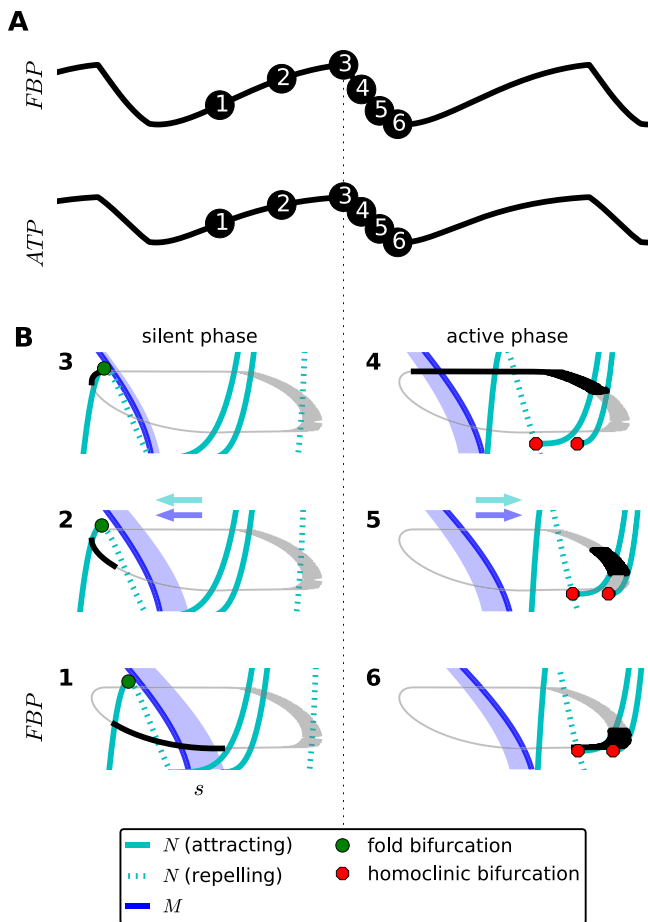
Fig. 9. The mechanism for sawtooth FBP oscillations in the IOM. (A) Sawtooth FBP and ATP oscillations with labels at time points during silent (labels 1–3) and active (labels 4–6) phases. (B) Phase portraits at the different time points, in the (s, FBP)-plane. The trajectory (segments shown in black) of the bursting attractor (gray) moves slowly along fast-subsystem equilibria (cyan) during the silent phase with small s before jumping to a branch of periodic spiking solutions (with large s) for the active phase. The fast-subsystem bifurcation diagram N moves leftward during the silent phase (left), and rightward during the active phase (right). The transformed ATP nullcline M has a similar motion. The blue curve shows its location at the current time point in each frame, while the shadow illustrates its motion since the last frame. (For interpretation of the references to colour in this figure legend, the reader is referred to the web version of this article.)

values results in sawtooth FBP oscillations that peak at the onset of the active phase. This is consistent with time series data of FBP levels in glucose-stimulated β-cells, where it was shown that the FBP level reliably peaked at the beginning of a burst active phase, while there was much greater variability in the timing of the FBP nadir Merrins et al. (2016). However, this approach to modeling Ca^{2+} regulation of PDH neglects the time required for Ca^{2+} concentration changes to affect the level of PDH activity.

We now ask how fast this Ca^{2+} effect must be to cause a decline in FBP level that begins at the onset of the active phase, as seen in experimental recordings. To answer this question, we add a differential equation to the IOM that governs the approach of s to the equilibrium $s_\infty(c_m)$ at a rate $\nu_s = \frac{1}{\tau_s}$:

$$\frac{ds}{dt} = \frac{s_\infty(c_m) - s}{\tau_s}, \tag{20}$$

where τ_s ranges from 1 ms to 1000 s, which encompasses the timescale of slow metabolic and fast electrical processes. We then record the resulting phase p ($p = 0$ corresponds to the onset of spiking and $p = 1$ corresponds to the end of spiking) at which
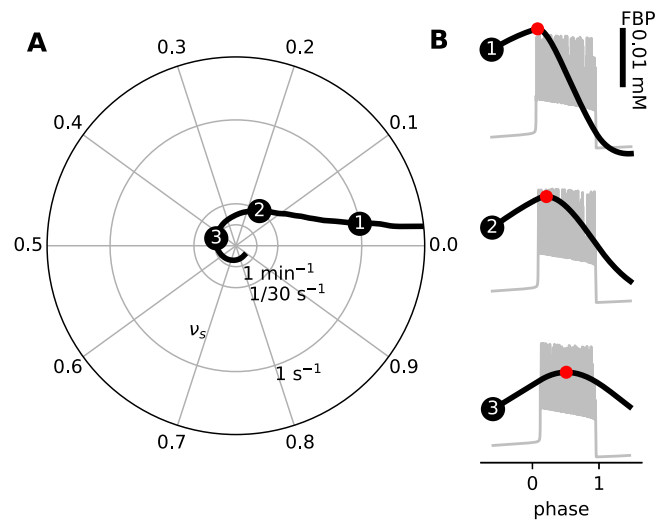
Fig. 10. (A) A polar plot of the relation between FBP peak phase p (0: beginning of active phase, 1: end of active phase) and ν_s in the IOM with angle $2\pi p$ and radius $\nu_s = 1/\tau_s$. (B) A representative burst for three different ν_s values. FBP peaks at phase $p = .03$, $p = .15$ and $p = .44$ for $\nu_s = 1$ s^{-1} (A1,B1), $\nu_s = 1/30$ s^{-1} (A2,B2), and $\nu_s = 1$ min^{-1} (A3,B3), respectively.

FBP peaks. Fig. 10A depicts this relation as a polar plot with angle $\theta = 2\pi p$ and radius $\nu_s = 1/\tau_s$. As ν_s is decreased, the FBP peak occurs later in the active phase, reflected by an increase in the angle θ. In particular, setting $\nu_s = 1$ s^{-1} results in FBP oscillations that peak at $p = .03$ (Fig. 10A1,B1), setting $\nu_s = 1/30$ s^{-1} results in $p = .15$ (Fig. 10A2,B2), and setting $\nu_s = 1$ min^{-1} results in $p = .44$ (Fig. 10A3,B3). We previously reported that FBP peaked at phase 0.011 ± 0.004 ($n = 47$) in glucose-stimulated islet β-cells Merrins et al. (2016). According to the relation depicted in Fig. 10A, the value of ν_s must be greater than 3 s^{-1}, or time constant $\tau_s < 333$ ms, to guarantee that FBP peaks before $p = .01$. Thus, the IOM predicts that Ca^{2+} regulation of PDH must occur on a fast timescale of less than half a second to cause FBP to decline at the onset of the active phase. This prediction could be tested by determining the rate at which the mitochondrial Ca^{2+} uniporter transports Ca^{2+} into β-cell mitochondria and by determining the rate at which mitochondrial dehydrogenase catalytic activity responds to step changes in the Ca^{2+} concentration.

Conclusions

Our main goal in this article was to characterize the mechanism for sawtooth FBP oscillations produced by the Integrated Oscillator Model (IOM) for pancreatic β-cells. This objective was motivated by a previously published pair of articles in which we argued, with support from FBP time series data, that Ca^{2+} regulation of mitochondrial dehydrogenases is the dominant form of Ca^{2+} feedback onto metabolism (Merrins et al., 2016) and that incorporating Ca^{2+} regulation of pyruvate dehydrogenase (PDH) into the Dual Oscillator Model, creating the IOM, produced sawtooth FBP oscillations (McKenna et al., 2016). In Fig. 1, we showed that when PDH is saturated by Ca^{2+}, FBP pulses that peak during the bursting active phase are produced but when there is no saturation, sawtooth FBP oscillations that peak at the onset of the active phase are produced. We showed (Fig. 2) that FBP pulses are produced by relaxation oscillations of the glycolytic subsystem that exist as long as glycolytic efflux balances glycolytic influx, and reducing the PDH saturation can prevent these relaxation oscillations (Figs. 3 and 4).

The sawtooth FBP oscillations that occur when the intrinsic glycolytic oscillations are not activated are due to Ca^{2+} feedback onto PDH that regulates glycolytic efflux. Changes in the Ca^{2+} concen-

tration that occur with a switch between silent and active phases of bursting dramatically move the equilibrium point of the glycolytic subsystem, so that the equilibrium is never reached. The FBP dynamics in this case reflect the movement of the phase point towards an equilibrium that is a moving target (Fig. 6). In terms of the reduced model (Fig. 5), this is a relaxation oscillation in which FBP is a slow variable and Ca^{2+} feedback onto PDH is the fast variable. Thus FBP takes on a sawtooth pattern (Fig. 7).

The full IOM also possesses these dynamics when Ca^{2+} feedback onto glycolysis is not saturated (Fig. 9), but the bursting electrical activity is best understood in terms of the action of ATP onto K(ATP) channels. Indeed, it is only through ATP (and the complementary ADP) that the glycolytic subsystem interacts with the electrical subsystem. Using a fast-slow analysis, we demonstrated that the fast subsystem of variables is bistable, and ATP periodically drives the system between the silent and the active states (Fig. 8). Since ATP is the slow process in this oscillation, it also takes on a sawtooth pattern.

Finally, we demonstrated that the Ca^{2+} feedback onto glycolysis must be rapid, with time constant less than half a second in our model, for the sawtooth FBP pattern to peak at the beginning of the burst active phase (Fig. 10). This is crucial, since experimental measurements of FBP have shown this behavior Merrins et al. (2016).

The analysis done here complements work of a companion paper Marinelli et al. (2018), which examined transitions between bursting oscillations driven by intrinsic glycolytic oscillations, and thus exhibiting a pulsatile FBP pattern, and those driven by Ca^{2+} feedback onto glycolysis and exhibiting a sawtooth FBP timecourse. The study shows that such transitions can be achieved by varying the strength of Ca^{2+} feedback onto glycolysis, similar to what we showed here, but also by changing an ionic conductance, which is not part of the glyoclytic subsystem. Importantly, it shows that compound bursting oscillations can also be produced, which have been frequently reported in electrical and Ca^{2+} measurements from islets (Arredouani et al., 2002; Bertram et al., 2007; Cook, 1983; Henquin et al., 1982). Together, the two papers illustrate that the IOM is capable of reproducing the key oscillatory behaviors of islet β-cells, with the intrinsic glycolytic oscillator sometimes activated and sometimes not.

Acknowledgments

Appendix A

A1. List of equations

In this section we give equations for the full model. A brief description of the model is given earlier, and a full description of the model is given in the companion paper Marinelli et al. (2018).

Table A1
Parameters for the electrical/calcium module.

$C = 5300$ fF	$g_{Ca} = 1000$ pS	$g_K = 2700$ pS
$g_{K(Ca)} = 1000$ pS	$g_{K(ATP)} = 26000$ pS	$V_{Ca} = 25$ mV
$V_K = -75$ mV	$v_m = -20$ mV	$s_m = 12$ mV
$v_n = -16$ mV	$s_n = 5$ mV	$\tau_n = 20$ ms
$k_d = 0.5\,\mu$M	$k_{dd} = 17\,\mu$M	$k_{tt} = 1\,\mu$M
$k_{td} = 26\,\mu$M	$f_{ca} = 0.01$	$\alpha = 5.18 \times 10^{-18}$ µmol fA^{-1} ms^{-1}
$V_{cyt} = 1.15 \times 10^{-12}$ l	$k_{PMCA} = 0.2$ ms^{-1}	$k_{SERCA} = 0.4$ ms^{-1}
$p_{leak} = 2 \times 10^{-4}$ ms^{-1}	$\sigma_{er} = 31$	

A2. The electrical and calcium module

Membrane potential:

$$\frac{dV}{dt} = -\frac{1}{C}\Big[I_{Ca} + I_K + I_{K(Ca)} + I_{K(ATP)}\Big] \tag{21}$$

Ca^{2+} current:

$$I_{Ca} = g_{Ca}m_\infty(V)(V - V_{Ca})$$

Instantaneous activation function for I_{Ca}:

$$m_\infty(V) = \frac{1}{1 + \exp[(v_m - V)/s_m]} \ . \tag{22}$$

Activation variable for I_K:

$$\frac{dn}{dt} = \frac{n_\infty(V) - n}{\tau_n}, \tag{23}$$

where $n_\infty(V)$ is a sigmoid of the form (22), but with shape parameters v_n and s_n.

Delayed rectifying K$^+$ current:

$$I_K = g_K n(V - V_K)$$

Ca^{2+}-activated K$^+$ current:

$$I_{K(Ca)} = g_{K(Ca)}q_\infty(c)(V - V_K) \tag{24}$$

Instantaneous activation function for $I_{K(Ca)}$:

$$q_\infty(c) = \frac{c^2}{k_d^2 + c^2}$$

ATP-sensitive K$^+$ current:

$$I_{K(ATP)} = g_{K(ATP)}o_\infty(ADP, ATP)(V - V_K) \tag{25}$$

Instantaneous activation function for $I_{K(ATP)}$:

$$o_\infty(ADP, ATP) = \frac{0.08 + 0.89\big(\frac{MgADP}{k_{dd}}\big)^2 + 0.16\big(\frac{MgADP}{k_{dd}}\big)}{\big(1 + \frac{MgADP}{k_{dd}}\big)^2\big(1 + \frac{ATP^{4-}}{k_{tt}} + \frac{ADP^{3-}}{k_{td}}\big)},$$

where $MgADP = 0.165ADP$, $ADP^{3-} = 0.135ADP$, and $ATP^{4-} = 0.05ATP$.

Free cytosolic Ca^{2+} concentration:

$$\frac{dc}{dt} = f_{Ca}(J_{mem} - J_{er}) \tag{26}$$

Ca^{2+} flux across plasma membrane:

$$J_{mem} = -\left[\frac{\alpha}{V_{cyt}}I_{Ca} + k_{PMCA}c\right] \tag{27}$$

Ca^{2+} flux across the endoplasmic reticulum (ER) membrane:

$$J_{er} = k_{SERCA}c - p_{leak}(c_{er} - c) \tag{28}$$

Free Ca^{2+} concentration in the ER:

$$\frac{dc_{er}}{dt} = f_{Ca}\sigma_{er}J_{er} \tag{29}$$

A3. The metabolic module

Cytosolic concentrations of fructose 6-phosphate (F6P) and fructose 1,6-bisphosphate (FBP):

$$\begin{aligned} \frac{dF6P}{dt} &= 0.3(J_{GK} - J_{PFK}) \\ \frac{dFBP}{dt} &= J_{PFK} - \tfrac{1}{2}J_{PDH} \end{aligned} \tag{30}$$

PFK reaction rate:

$$J_{PFK} = v_{PFK}\frac{w_{1110} + k_{PFK}\sum_{i,j,l\in\{0,1\}} w_{ij1l}}{\sum_{i,j,k,l\in\{0,1\}} w_{ijkl}} \tag{31}$$

Table A2
Parameters for the metabolic module.

$J_{GK} = 0.001\,\mu M\,ms^{-1}$	$v_{PFK} = 0.01\,\mu M\,ms^{-1}$	$k_{PFK} = 0.06$	$K_1 = 30\,\mu M$
$K_2 = 1\,\mu M$	$K_3 = 5 \times 10^4\,\mu M$	$K_4 = 10^3\,\mu M$	$f_{13} = 0.02$
$f_{23} = 0.2$	$f_{41} = 20$	$f_{42} = 20$	$f_{43} = 20$
$v_{PDH} = 0.001\,\mu M\,ms^{-1}$	$K_{PDH}^{Ca} = 1\,\mu M$	$\tau_a = 300000\,ms$	$A_{tot} = 3000\,\mu M$

with weights

$$w_{ijkl} = \frac{(AMP/K_1)^i (FBP/K_2)^j (F6P/K_3)^k (ATP/K_4)^l}{f_{13}^{ik} f_{23}^{jk} f_{41}^{il} f_{42}^{jl} f_{43}^{kl}} \tag{32}$$

where $AMP = \frac{ADP^2}{ATP}$.

PDH reaction rate:

$$J_{PDH} = v_{PDH} s_\infty(c_m) \sqrt{FBP} \tag{33}$$

or

$$J_{PDH} = v_{PDH} s \sqrt{FBP} \tag{34}$$

Equilibrium flux function for PDH:

$$s_\infty(c_m) = \frac{c_m}{K_{PDH} + c_m} \tag{35}$$

ADP concentration:

$$\frac{dADP}{dt} = \frac{\left\{ ATP - \exp\left[\left(1 + 2.2\frac{J_{PDH}}{0.05 + J_{PDH}}\right)\left(1 - \frac{c}{0.35}\right)\right] ADP \right\}}{\tau_a} \tag{36}$$

ATP concentration:

$$ATP = \frac{1}{2}\left[A_{tot} + \sqrt{-4ADP^2 + (A_{tot} - ADP)^2} - ADP \right] \tag{37}$$

where A_{tot} is the total nucleotide concentration.

A4. Time scale analysis

The variables in the model evolve over a large range of time scales. We partition then into three classes, based on the time scale analysis below.

V time scale:

Define the dimensionless voltage $\bar{V} = \frac{V}{k_V}$ where $k_V = 100$ mV is a typical voltage scale. Then define a dimensionless time variable $\tau = \frac{t}{k_t}$ where $k_t = 60,000$ ms (1 min) is a typical slow time scale. Let g_{max} be an upper bound on the total conductance of the ion channels during slow bursting oscillations. That is, an upper bound on $g_{Ca}m_\infty + g_K n + g_{K(Ca)}q_\infty + g_{K(ATP)}o_\infty$. We use $g_{max} = 1000$ pS. The membrane time constant is then $\tau_V = \frac{C}{g_{max}} \approx 5.3$ ms. The dimensionless conductances have the form $\bar{g}_x = \frac{g_x}{g_{max}}$. Then the dimensionless V equation is

$$\frac{d\bar{V}}{d\tau} = -\frac{1}{\bar{\tau}_V} \sum \bar{I}, \tag{38}$$

where $\sum \bar{I}$ is the sum of the currents (as in Eq. 21), where each current is dimensionless and is $\mathcal{O}(1)$. For example, $\bar{I}_{Ca} = \bar{g}_{Ca}m_\infty(\bar{V} - \bar{V}_{Ca})$, where $\bar{V}_{Ca} = \frac{V_{Ca}}{k_V}$. The dimensionless V time scale is then $\bar{\tau}_V = \frac{\tau_V}{k_t} \approx 10^{-4}$.

n time scale:

The dimensionless n differential equation is

$$\frac{dn}{d\tau} = \frac{1}{\bar{\tau}_n}(n_\infty - n), \tag{39}$$

where the dimensionless n time scale is $\bar{\tau}_n = \frac{\tau_n}{k_t} \approx 3 \times 10^{-4}$.

c time scale:

Define $k_c = 0.2$ μM as an upper bound on the free Ca^{2+} concentration during slow bursting. The dimensionless c is $\bar{c} = \frac{c}{k_c}$. Let k_1 be an upper bound on the absolute value of the Ca^{2+} flux $J_{mem} - J_{er}$

during slow bursting. We use $k_1 = 0.1$ μM/ms. Then the dimensionless c differential equation is:

$$\frac{d\bar{c}}{d\tau} = \frac{1}{\bar{\tau}_c}(\bar{J}_{mem} - \bar{J}_{er}), \tag{40}$$

where $\bar{J}_x = \frac{J_x}{k_1}$, and where the dimensionless c time scale is $\bar{\tau}_c = \frac{k_c}{k_1 k_t f_{Ca}} \approx 3 \times 10^{-3}$.

c_{er} time scale:

Define $k_{er} = 350$ μM as an upper bound on the free Ca^{2+} concentration in the ER during slow bursting. The dimensionless c_{er} is then $\bar{c}_{er} = \frac{c_{er}}{k_{er}}$. The flux of Ca^{2+} into the ER during slow bursting has an upper bound of $k_2 = 0.025$ μM/ms, so the dimensionless flux can be defined as $\bar{J}_{er} = \frac{J_{er}}{k_2}$. The dimensionless c_{er} differential equation is then

$$\frac{d\bar{c}_{er}}{d\tau} = \frac{1}{\bar{\tau}_{er}}\bar{J}_{er}, \tag{41}$$

where the dimensionless c_{er} time scale is $\bar{\tau}_{er} = \frac{k_{er}}{k_t f_{Ca} k_2 \sigma_{er}} \approx 0.75$.

F6P time scale:

Define $k_{F6P} = 30$ μM as an upper bound on the F6P concentration during the slow bursting produced with $K_{PDH}^{Ca} = 1$ μM. The dimensionless F6P concentration is then $\bar{F6P} = \frac{F6P}{k_{F6P}}$. The difference $J_{GK} - J_{PFK}$ is bounded above by $k_3 = 10^{-4}$ μM/ms. The dimensionless F6P differential equation is then

$$\frac{d\bar{F6P}}{d\tau} = \frac{1}{\bar{\tau}_{F6P}}(\bar{J}_{GK} - \bar{J}_{PFK}), \tag{42}$$

where $\bar{J}_x = \frac{J_x}{k_3}$ and the dimensionless F6P time scale is $\bar{\tau}_{F6P} = \frac{k_{F6P}}{0.3 k_3 k_t} \approx 17$.

FBP time scale:

Define $k_{FBP} = 60$ μM as an upper bound on the FBP concentration during slow bursting produced with $K_{PDH}^{Ca} = 1$ μM. The dimensionless FBP concentration is then $\bar{FBP} = \frac{FBP}{k_{FBP}}$. The difference $J_{PFK} - \frac{1}{2}J_{PDH}$ is bounded above by $k_4 = 5 \times 10^{-4}$ μM/ms. The dimensionless FBP differential equation is then

$$\frac{d\bar{FBP}}{d\tau} = \frac{1}{\bar{\tau}_{FBP}}\left(\bar{J}_{PFK} - \frac{1}{2}\bar{J}_{PDH}\right), \tag{43}$$

where $\bar{J}_x = \frac{J_x}{k_4}$ and the dimensionless FBP time scale is $\bar{\tau}_{FBP} = \frac{k_{FBP}}{k_4 k_t} \approx 2$.

ADP time scale:

Define $k_{ADP} = 900$ μM as an upper bound on the ADP concentration during slow bursting. The dimensionless ADP concentration is then $\bar{ADP} = \frac{ADP}{k_{ADP}}$. Define the function $F = \left\{ ATP - \exp\left[\left(1 + 2.2\frac{J_{PDH}}{0.05 + J_{PDH}}\right)\left(1 - \frac{c}{0.35}\right)\right] ADP \right\}$, the numerator in the right hand side of Eq. (36). This function has an upper bound of $k_5 = 400$ μM during slow bursting. The dimensionless ADP differential equation is then

$$\frac{d\bar{ADP}}{d\tau} = \frac{1}{\bar{\tau}_{ADP}}\bar{F}, \tag{44}$$

where $\bar{F} = \frac{F}{k_5}$ and the dimensionless ADP time scale is $\bar{\tau}_{ADP} = \frac{k_{ADP}\tau_a}{k_5 k_t} \approx 11$.

ATP time scale:

ATP is related algebraically to ADP through Eq. (37). Define $k_{\text{ATP}} = 1800\,\mu\text{M}$ as an upper bound on the ATP concentration during slow bursting. The dimensionless ATP concentration is then $\bar{\text{ATP}} = \frac{\text{ATP}}{k_{\text{ATP}}}$. With the usual definition for dimensionless time constant τ, the rate of change of $\bar{\text{ATP}}$ with respect to τ is then

$$\frac{d\bar{\text{ATP}}}{d\tau} = \left(\frac{d\text{ATP}}{d\text{ADP}}\right)\left(\frac{k_{\text{ADP}}}{k_{\text{ATP}}}\right)\left(\frac{1}{\bar{\tau}_{\text{ADP}}}\bar{F}\right) \tag{45}$$

The derivative $\frac{d\text{ATP}}{d\text{ADP}}$ can be computed from Eq. (37),

$$\frac{d\text{ATP}}{d\text{ADP}} = -\frac{1}{2}\left(\frac{3\text{ADP} + A_{\text{tot}}}{\sqrt{-4\text{ADP}^2 + (A_{\text{tot}} - \text{ADP})^2}} + 1\right) \tag{46}$$

and during slow bursting $\frac{d\text{ATP}}{d\text{ADP}} \approx -\frac{1}{2}$. Thus,

$$\frac{d\bar{\text{ATP}}}{d\tau} \approx \left(\frac{-1}{2}\right)\left(\frac{900}{1800}\right)\left(\frac{1}{\bar{\tau}_{\text{ADP}}}\bar{F}\right) \tag{47}$$

and therefore the dimensionless ATP time scae is $\bar{\tau}_{\text{ATP}} \approx 4\bar{\tau}_{\text{ADP}} = 44$.

s time scale:

In most of the analysis s is assumed to be at quasi-steady state. However, in the last section of Results its dynamics are described by a differential equation (Eq. 20). In this case, the dimensionless s differential equation is

$$\frac{ds}{d\tau} = \frac{1}{\bar{\tau}_s}(s_\infty - s), \tag{48}$$

where the dimensionless s time scale is $\bar{\tau}_s = \frac{\tau_s}{k_t}$. The time constant τ_s is varied from 10^{-3} to 10^3 s, so the dimensionless s time constant varies from $\approx 10^{-8}$ to 10^{-2}.

Time scale classification:

From this analysis, we partition the variables into fast (V, n, c, s), medium (c_{er} and FBP), and slow (F6P, ADP or ATP).

References

Arredouani, A., Henquin, J.-C., Gilon, P., 2002. Contribution of the endoplasmic reticulum to the glucose-induced [Ca^{2+}]$_c$ response in mouse pancreatic islets. Am. J. Physiol. 1330, E982–E991.

Bertram, R., Rubin, J., 2017. Multi-timescale systems and fast-slow analysis. Math. Biosci. 287, 105–121.

Bertram, R., Satin, L., Sherman, A., 2018. Closing in on the mechanisms of pulsatile insulin secretion. Diabetes 67, 351–359.

Bertram, R., Satin, L., Zhang, M., Smolen, P., Sherman, A., 2004. Calcium and glycolysis mediate multiple bursting modes in pancreatic islets. Biophys. J. 87 (5), 3074–3087.

Bertram, R., Sherman, A., Satin, L., 2007. Metabolic and electrical oscillations: partners in controlling pulsatile insulin secretion. Am. J. Physiol. 293, E890–E900.

Bratusch-Marrain, P., Komjati, M., Waldhäusl, W.K., 1986. Efficacy of pulsatile versus continuous insulin administration on hepatic glucose production and glucose utilization in type i diabetic humans. Diabetes 35 (8), 922–926.

Cook, D.L., 1983. Isolated islets of langerhans have slow oscillations of electrical activity. Metabolism 32, 681–685.

Denton, R.M., 2009. Regulation of mitochondrial dehydrogenases by calcium ions. Biochim. Biophys. Acta Bioenerg. 1787 (11), 1309–1316.

Henquin, J.C., Meissner, H.P., Schmeer, W., 1982. Cyclic variations of glucose-induced electrical activity in pancreatic β cells. Pflügers Arch. 393, 322–327.

Hodgkin, A.L., Huxley, A.F., 1952. A quantitative description of membrane current and its application to conduction and excitation in nerve. J. Physiol 117, 500–544.

Keizer, J., Magnus, G., 1989. ATP-Sensitive potassium channel and bursting in the pancreatic β cell. Biophys. J. 56, 229–242.

Komjati, M., Bratusch-Marrain, P., Waldhäusl, W., 1986. Superior efficacy of pulsatile versus continuous hormone exposure on hepatic glucose production in vitro. Endocrinology 118 (1), 312–319.

Lillioja, S., Mott, D.M., Spraul, M., Ferraro, R., Foley, J.E., Ravussin, E., Knowler, W.C., Bennett, P.H., Bogardus, C., 1993. Insulin resistance and insulin secretory dysfunction as precursors of non-insulin-dependent diabetes mellitus: prospective studies of pima indians. New Eng. J. Med. 329 (27), 1988–1992.

Marinelli, I., Vo, T., Gerardo-Giorda, L., Bertram, R., 2018. Transitions between bursting modes in the integrated oscillator model for pancreatic β-cells. J. Theor. Biol. 454, 310–319.

Matveyenko, A.V., Liuwantara, D., Gurlo, T., Kirakossian, D., Dalla Man, C., Cobelli, C., White, M.F., Copps, K.D., Volpi, E., Fujita, S., et al., 2012. Pulsatile portal vein insulin delivery enhances hepatic insulin action and signaling. Diabetes 61 (9), 2269–2279.

McKenna, J.P., Ha, J., Merrins, M.J., Satin, L.S., Sherman, A., Bertram, R., 2016. Ca^{2+} effects on ATP production and consumption have regulatory roles on oscillatory islet activity. Biophys. J. 110 (3), 733–742.

Merrins, M.J., Poudel, C., McKenna, J.P., Ha, J., Sherman, A., Bertram, R., Satin, L.S., 2016. Phase analysis of metabolic oscillations and membran potential in pancreatic islet β-cells. Biophys. J. 110, 691–699.

Merrins, M.J., Van Dyke, A.R., Mapp, A.K., Rizzo, M.A., Satin, L.S., 2013. Direct measurements of oscillatory glycolysis in pancreatic islet β-cells using novel fluorescence resonance energy transfer (FRET) biosensors for pyruvate kinase M2 activity. J. Biol. Chem. 288 (46), 33312–33322.

Nunemaker, C.S., Satin, L.S., 2014. Episodic hormone secretion: a comparison of the basis of pulsatile secretion of insulin and GnRH. Endocrine 47, 49–63.

O'Rahilly, S., Turner, R.C., Matthews, D.R., 1988. Impaired pulsatile secretion of insulin in relatives of patients with non-insulin-dependent diabetes. N. Engl. J. Med. 318 (19), 1225–1230.

Polonsky, K.S., Given, B.D., Hirsch, L.J., Tillil, H., Shapiro, E.T., Beebe, C., Frank, B.H., Galloway, J.A., Van Cauter, E., 1988. Abnormal patterns of insulin secretion in non-insulin-dependent diabetes mellitus. N. Engl. J. Med. 318 (19), 1231–1239.

Sherman, A., 2010. Lessons from models of β-cells for engineering glucose-sensing cells. Math. Biosci. 227, 12–19.

Smolen, P., 1995. A model for glycolytic oscillations based on skeletal muscle phosphofructokinase kinetics. J. Theor. Biol. 174, 137–148.

Westermark, P.O., Lansner, A., 2003. A model of phosphofructokinase and glycolytic oscillations in the pancreatic β-cell. Biophys. J. 85 (1), 126–139.

Wiederkehr, A., Szanda, G., Akhmedov, D., Mataki, C., Heizmann, C.W., Schoonjans, K., Pozzan, T., Spät, A., Wollheim, C.B., 2011. Mitochondrial matrix calcium is an activating signal for hormone secretion. Cell Metab. 13 (5), 601–611.